Available online at www.sciencedirect.com

ScienceDirect

International Journal of Heat and Mass Transfer 50 (2007) 2217–2235

International Journal of HEAT and MASS TRANSFER

www.elsevier.com/locate/ijhmt

Effects of electromagnetic force on melt flow and porosity prevention in pulsed laser keyhole welding

Jun Zhou, Hai-Lung Tsai *

Laser-Based Manufacturing Laboratory, Department of Mechanical and Aerospace Engineering, University of Missouri-Rolla,
1870 Miner Circle, Rolla, MO 65409-1350, United States

Received 13 March 2006; received in revised form 28 October 2006
Available online 29 December 2006

Abstract

Porosity formation in pulsed laser keyhole welding was found to be affected by two competing factors: (1) the solidification rate of molten metal and (2) the back filling speed of molten metal during the keyhole collapse process. Porosity (pores/voids) was found in welds when the solidification rate of molten metal exceeds the back filling speed of molten metal. In this study, the use of electromagnetic force was proposed to control the back filling speed of molten metal, and a mathematical model was developed to investigate the effects of electromagnetic force on the transient melt flow, keyhole dynamics, and porosity formation. The results demonstrate that porosity in pulsed laser welding can be prevented by an applied electromagnetic force. Parametric studies to determine the desired strength of the electromagnetic force and its duration were also conducted to achieve quality welds.

Keywords: Laser welding; Electromagnetic force; Keyhole; Porosity prevention

---

1. Introduction

Lasers have achieved increased significance for welding in recent years for their high power density and the resulting small heat-affected zone in welds. Especially, with high depth-to-width aspect ratio and high welding speed, laser keyhole welding is more promising compared to conventional welding processes. However, in deep penetration laser welds, pores/voids (porosity) are frequently observed [1–4] which deteriorate the strength of the weld. In order to optimize a laser welding process and to ensure high weld quality and strength, it is necessary to understand the porosity formation mechanism in pulsed laser welding and to find methods to reduce or eliminate porosity defects.

Over the years, a number of researchers have conducted experiments to investigate porosity formation in pulsed laser welding [5–7]. Based on these experimental observations, it was found that the formation of porosity has a close relationship with keyhole dynamics and the collapse of the keyhole right after the termination of laser irradiation. In pulsed laser welding, during the keyhole formation process, molten metal is squeezed outward and upward, surrounding the upper portion of the keyhole. Once the laser irradiation is terminated, the melt in the upper part of the keyhole flows downward to fill the keyhole. At the same time, the upper part of the melt rapidly solidifies which prevents the melt from flowing to fill the keyhole, leading to the formation of porosity (pores). Note porosity can also be caused by the entrainment of shielding gas and/or the dissolution of gas (for example, hydrogen) during the solidification process which is normally called gas porosity [8–10]. This study is limited to the porosity that is caused by the failure of back filling the keyhole due to premature solidification of molten metal which can occur when the keyhole is relatively deep in pulsed laser keyhole welding.

Zhou et al. [11,12] developed mathematical models to investigate the keyhole dynamics, heat transfer and fluid flow, and the porosity formation process in pulsed laser

---

* Corresponding author. Tel.: +1 573 341 4945; fax: +1 573 341 4607.
E-mail address: tsai@umr.edu (H.-L. Tsai).

0017-9310/$ - see front matter © 2006 Elsevier Ltd. All rights reserved.
doi:10.1016/j.ijheatmasstransfer.2006.10.040

Nomenclature

A	constant in Eq. (14)
A_v	constant in Eq. (18)
$\boldsymbol{B}$	magnetic flux vector
B_0	constant in Eq. (14)
B_θ	magnetic flux density
c_p	specific heat of metal
c_{pl}	specific heat of plasma
c	the speed of light
C	coefficient in Eqs. (2) and (3)
e	charge of electron
E_i	ionization potential for neutral atom
f^α	sulfur concentration in base metal
F	volume of fluid function
g	gravitational acceleration
g_e	degeneracy factor of electron particle
g_i	degeneracy factor of ion particle
g_0	degeneracy factor of neutral atom
$\bar{g}$	quantum mechanical Gaunt factor
h	enthalpy for metal
h_{pl}	enthalpy for plasma
h_{conv}	convective heat transfer coefficient
$\bar{h}$	Planck's constant
H_v	latent heat for liquid–vapor
H_b	thickness of base metal
$I(\boldsymbol{r}, \boldsymbol{s})$	total directional radiative intensity
I_b	black body emission intensity
$I_c(r)$	collimate incident laser beam intensity distribution on the focus plane
$I_0(r, z)$	incident intensity from laser beam
$I_{r,m}(r, z)$	incident intensity from mth reflection
$\boldsymbol{J}$	electric current flux vector
j_r	electric current density in r-direction
j_z	electric current density in z-direction
k_a	Planck mean absorption coefficient
k_b	Boltzmann constant
k_{pl}	thermal conductivity of plasma
k	thermal conductivity of metal
K	permeability function in Eqs. (2) and (3)
K_{pl}	inverse Bremsstrahlung (IB) absorption coefficient
m_a	atomic mass
m_e	electron mass
m_v	variable defined in Eq. (42)
m	constant in Eq. (24)
M_K	Mach number at the outer of the Knudsen layer
$\vec{n}$	vector normal to local free surface
n_e	electron density in plasma
n_i	ion density in plasma
n_0	neutral particle density in plasma
N_a	Avogadro's number
p	pressure in liquid metal
P_{laser}	laser power
P_r	recoil pressure
P_σ	surface tension
q_{conv}	heat loss by convection
q_{evap}	heat loss by evaporation
q_{laser}	heat flux by laser irradiation
q_{rad}	heat loss by radiation
$\boldsymbol{q}_r$	radiation heat flux vector
r–z	cylindrical coordinate system
r_f	laser beam radius
r_{fo}	laser beam radius at the focal position
R	gas constant
R_b	radius of base metal
$\vec{s}$	vector tangential to local free surface
t	time
T	temperature of metal
T_0	reference temperature
T_K	plasma temperature outside of Knudsen layer
T_{pl}	temperature of plasma
$\overline{T}_{pl}$	average plasma temperature
T_w	surface temperature of the liquid metal at the keyhole wall
T_∞	ambient temperature
u	velocity in r-direction
U	variable defined in Eq. (15)
v	velocity in z-direction
$\boldsymbol{V}$	velocity vector
$\boldsymbol{V}_r$	relative velocity vector ($\boldsymbol{V}_l - \boldsymbol{V}_s$)
W	melt mass evaporation rate
Z	charge of ion

Greek symbols

ϕ	scalar electrical potential
α_{Fr}	Fresnel absorption coefficient
β_T	thermal expansion coefficient
$\partial\gamma/\partial T$	surface tension temperature gradient
ε	surface radiation emissivity
ε_0	dielectric constant
ε_f	constant in Eq. (20)
γ	surface tension coefficient
γ_r	specific heat ratio
ω	angular frequency of laser irradiation
Ω	solid angle
κ	free surface curvature
μ_l	dynamic viscosity
σ	Stefan–Boltzmann constant
σ_e	electrical conductivity
ϕ	angle of incident laser light
ρ	density of metal
ρ_{pl}	density of plasma
$\tau_{\vec{s}}$	Marangoni shear stress

Subscripts

0	initial value
c	original incident laser light

l	liquid phase
r	relative to solid velocity
(r, m)	mth reflected laser beam
pl	plasma
s	solid phase

welding. Their studies indicate that porosity formation is affected by two competing factors. One is the solidification rate of the molten metal and the other is the back filling speed of the molten metal during the keyhole collapse process. Porosity was found in the final weld when the solidification rate of the molten metal exceeds the back filling speed of liquid metal. Porosity formation has a close relationship with the depth-to-width aspect ratio of the keyhole in pulsed laser keyhole welding. The larger the aspect ratio, the easier the porosity and the larger the size of the pore/void is formed. To reduce/eliminate the pore/void in the weld, a method was proposed to delay the solidification process by controlling the pulse shape of the laser irradiation [7,10,12]. This method prolongs the solidification rate and is effective in preventing/eliminating porosity for medium depth-to-width aspect ratio laser keyhole welding. However, it failed for a keyhole with large depth-to-width aspect ratio [10,12].

In this study, a new method is proposed to control the back filling melt flow during the keyhole collapse process. This can be achieved by increasing the back filling speed of the molten metal via the application of an electromagnetic force (Lorentz force). Electromagnetic force has been found to be able to affect melting and solidification processes [13–15] and has been used in arc welding to change flow conditions [16–19]. In arc welding, when an electric current flows through the workpiece, it will interact with a magnetic field to generate an electromagnetic force. This electromagnetic force can change the momentum of the melt flow and to avoid weld slag or droplet detachment under the effect of gravitation when welding in a “wall position” [16,17]. In gas metal arc welding (GMAW), temperature and velocity fields, weld pool geometry and thermal cycles were also observed to be strongly influenced by electromagnetic force [18]. Recently, experimental studies have been conducted to investigate the usage of electromagnetic force in laser welding [20,21]. Electromagnetic force was found to be able to affect the melt flow and weld pool dynamics in laser welding to achieve good quality welds.

Although experimental observations can provide some useful information, the underlying physics, such as temperature and velocity evolutions during the keyhole formation and collapse cannot be revealed. This is especially true for the phenomena that occur inside the keyhole. However, the temperature and velocity evolutions during the keyhole collapse and the solidification processes play a significant role on the formation of porosity. In this paper, mathematical models are developed to study the interplay between the electromagnetic force and the keyhole dynamics, melt flow and heat transfer in pulsed laser keyhole welding. Parametric studies are also conducted to investigate the effectiveness of the electromagnetic force on porosity prevention and to determine the desired strength and duration of the electromagnetic force to achieve quality welds.

2. Mathematical model

Fig. 1 shows a schematic sketch of a pulsed laser keyhole welding process. A control volume method employing the volume of fluid (VOF) technique [22] and the continuum formulation [23] is used to calculate the momentum and energy transport in the weld pool. The VOF technique can handle a transient deformed weld pool surface, while the continuum formulation can handle fusion and solidification for the liquid region, the mush zone and the solid region. Plasma in the keyhole is treated as the vapor of weld material. Although the velocity and pressure change dramatically across the Knudsen layer, the generic translation vapor flow along the keyhole is neglected [24] and, in the present study, only the temperature distribution is considered. Meanwhile, the pressure along the keyhole is considered to be approximately constant [25] and is comparable to the atmospheric pressure. Note in high power laser welding ($\geqslant 8$ kW), the plasma plume and its velocities in the keyhole can be very significant [4,5] and, hence, the assumption of no plasma flow in the present study is limited to low power laser keyhole welding.

2.1. Metal zone simulation

2.1.1. Governing equations

The governing differential equations used to describe the heat and mass transfer and fluid flow in a cylindrical coordinate (r–z) system given by Chiang and Tsai [23] are modified and used in the present study:

Continuity

$$\frac{\partial}{\partial t}(\rho) + \nabla \cdot (\rho \boldsymbol{V}) = 0 \tag{1}$$

Momentum

$$\begin{aligned}\frac{\partial}{\partial t}(\rho u) + \nabla \cdot (\rho \boldsymbol{V} u) &= \nabla \cdot \left(\mu_l \frac{\rho}{\rho_l} \nabla u\right) - \frac{\partial p}{\partial r} - \frac{\mu_l}{K} \frac{\rho}{\rho_l}(u - u_s) \\ &\quad - \frac{C\rho^2}{K^{0.5}\rho_l}|u - u_s|(u - u_s) - \nabla \cdot (\rho f_s f_l \boldsymbol{V}_r u_r) \\ &\quad + \nabla \cdot \left(\mu_s u \nabla\left(\frac{\rho}{\rho_l}\right)\right) + \boldsymbol{J} \times \boldsymbol{B}|_r\end{aligned} \tag{2}$$

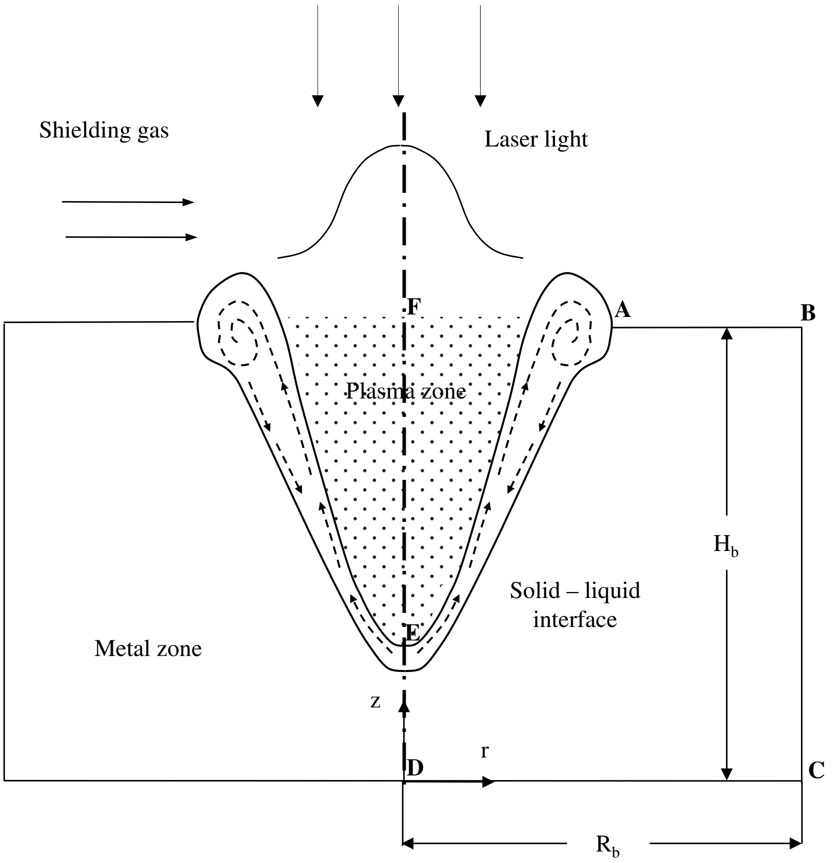

Fig. 1. Schematic sketch of the pulsed laser keyhole welding process.

$$
\begin{aligned}
&\frac{\partial}{\partial t}(\rho v)+\nabla\cdot(\rho V v)\\
&\quad=\rho g+\nabla\cdot\left(\mu_{\mathrm{l}}\frac{\rho}{\rho_{\mathrm{l}}}\nabla v\right)-\frac{\partial p}{\partial z}-\frac{u_{\mathrm{l}}}{K}\frac{\rho}{\rho_{\mathrm{l}}}(v-v_{\mathrm{s}})\\
&\qquad-\frac{C\rho^2}{K^{0.5}\rho_{\mathrm{l}}}|v-v_{\mathrm{s}}|(v-v_{\mathrm{s}})-\nabla\cdot(\rho f_{\mathrm{s}}f_{\mathrm{l}}\boldsymbol{V}_r v_r)\\
&\qquad+\nabla\cdot\left(\mu_{\mathrm{s}}v\nabla\left(\frac{\rho}{\rho_{\mathrm{l}}}\right)\right)+\rho g\beta_{\mathrm{T}}(T-T_0)+\boldsymbol{J}\times\boldsymbol{B}|_z \qquad (3)
\end{aligned}
$$

Energy

$$
\begin{aligned}
\frac{\partial}{\partial t}(\rho h)+\nabla\cdot(\rho V h)=\nabla\cdot\left(\frac{k}{c_p}\nabla h\right)-\nabla\cdot\left(\frac{k}{c_p}\nabla(h_{\mathrm{s}}-h)\right)\\
-\nabla\cdot(\rho(\boldsymbol{V}-\boldsymbol{V}_{\mathrm{s}})(h_{\mathrm{l}}-h)) \qquad (4)
\end{aligned}
$$

The physical meaning of each term appearing in the above equations can be found in Ref. [23]. In Eqs. (1)–(4) the continuum density, specific heat, thermal conductivity, solid mass fraction, liquid mass fraction, velocity and enthalpy are defined in Ref. [26]. The last term in Eqs. (2) and (3) represents the electromagnetic force in the r- and z-direction, respectively. Before electromagnetic force is applied, these two items are zero and they are treated as body forces after the electromagnetic force is applied. The calculation of electromagnetic forces is in the following:

$$
\boldsymbol{J}\times\boldsymbol{B}|_r=-j_r B_\theta,\quad \boldsymbol{J}\times\boldsymbol{B}|_z=j_z B_\theta \qquad (5)
$$

where j_r and j_z are the current density in r- and z-direction, respectively. In order to have the flexibility of controlling the magnitude and direction of the resulting electromagnetic force, an electrical potential and a magnetic field are applied independently. Based on our previous studies [27], since the self-induced magnetic field intensity caused by the external electrical current is much smaller than the externally applied magnetic field intensity, its effect is neglected. Hence, B_θ in Eq. (5) represents the externally applied magnetic flux density. The electrical current density can be calculated in the following:

Conservation of current

$$
\frac{1}{r}\frac{\partial}{\partial r}\left(\sigma_{\mathrm{e}} r\frac{\partial\phi}{\partial r}\right)+\frac{\partial}{\partial z}\left(\sigma_{\mathrm{e}}\frac{\partial\phi}{\partial z}\right)=0 \qquad (6)
$$

where σ_{e} is electrical conductivity and ϕ is electrical potential. According to Ohm's law, the electrical current density in r- and z-direction is defined as

$$
j_r=-\sigma_{\mathrm{e}}\frac{\partial\phi}{\partial r},\quad j_z=-\sigma_{\mathrm{e}}\frac{\partial\phi}{\partial z} \qquad (7)
$$

2.1.2. Tracking of free surfaces

The algorithm of volume-of-fluid (VOF) is used to track the dynamics of free surfaces [22]. The fluid configuration is defined by a volume of fluid function, $F(r,z,t)$, which tracks the location of free surface. The function F takes the value of one for the cell full of fluid and the value of zero for the empty cell. Cells with F values between zero and one are partially filled with fluid and identified as surface cells. The function F is governed by the following equation:

$$\frac{\mathrm{d}F}{\mathrm{d}t} = \frac{\partial F}{\partial t} + (\boldsymbol{V} \cdot \nabla)F = 0 \tag{8}$$

Table 1
Boundary conditions (as shown in Fig. 3) for Eq. (6)

Boundaries	AB	BC	CD	DE	EA
$B \cdot C \cdot s$	$-\sigma_e \frac{\partial \phi}{\partial z} = \frac{I}{\pi R_2^2}$	$\frac{\partial \phi}{\partial z} = 0$	$\frac{\partial \phi}{\partial r} = 0$	$\phi = 0$	$\frac{\partial \phi}{\partial r} = 0$

Where R_2 is the radius of the electrode as shown in Fig. 3.

2.1.3. Boundary conditions

The boundaries of the metal zone simulation are divided into five segments, as shown in Fig. 1.

Table 2
Thermophysical properties of 304 stainless steel and process parameters

Nomenclature	Value
Constant in Eq. (14), A (Pa)	0.55
Constant in Eq. (18), A_v	2.52
Vaporization constant in Eq. (14), B_0	1.78×10^{10}
Speed of light, c (m s^{-1})	3×10^{8}
Specific heat of solid phase, c_s (J kg^{-1} K^{-1})	700
Specific heat of liquid phase, c_l (J kg^{-1} K^{-1})	780
Specific heat of plasma, c_{pl} (J kg^{-1} K^{-1})	49.0
Charge of electron, e (C)	1.6022×10^{-19}
Ionization potential for neutral atoms, E_i (J)	1.265×10^{-18}
Sulfur concentration in base metal, f^{α} (ppm)	100
Gravitational acceleration, g (m s^{-2})	9.8
Degeneracy factors for electrons, g_e	30
Degeneracy factors for ions, g_i	30
Degeneracy factors for neutral atoms, g_0	25
Quantum mechanical Gaunt factor, $\bar{g}$	1.5
Convective heat transfer coefficient, h_{conv} (W m^{-2} K^{-1})	80
Planck's constant, $\bar{h}$ (J s)	6.625×10^{-34}
Latent heat of fusion, H (J kg^{-1})	2.47×10^{5}
Thickness of substrate metal, H_b (mm)	3.0
Latent heat of vaporization, H_v (J kg^{-1})	6.34×10^{6}
Boltzmann constant, k_b (J K^{-1})	1.38×10^{-23}
Thermal conductivity of liquid phase, k_l (W m^{-1} K^{-1})	22
Thermal conductivity of plasma, k_{pl} (W m^{-1} K^{-1})	3.74
Thermal conductivity of solid phase, k_s (W m^{-1} K^{-1})	22
Atomic mass, m_a (g)	9.3×10^{-23}
Electron mass, m_e (g)	9.1×10^{-28}
Mach number at the outer of the Knudsen layer, M_K	1.2
Avogadro's number, N_a (mol^{-1})	6.022×10^{23}
Laser power, P_{laser} (W)	1700
Laser beam radius, r_f (mm)	0.25
Laser beam radius at focus, r_{f0} (mm)	0.25
Gas constant, R (J kg^{-1} mol^{-1})	8.3×10^{3}
Radius of substrate metal, R_b (mm)	20.0
Liquidus temperature, T_l (K)	1780
Reference temperature, T_0 (K)	1700
Solidus temperature, T_s (K)	1670
Ambient temperature, T_∞ (K)	300
Average ionic charge in the plasma, Z	1
Thermal expansion coefficient, β_T (K^{-1})	4.95×10^{-5}
Surface radiation emissivity, ε	0.4
Dielectric constant, ε_0	14.2
Constant in Eq. (20), ε_f	0.2
Specific heat ratio, γ_r	1.67
Angular frequency of laser radiation, ω (rad s^{-1})	1.78×10^{14}
Dynamic viscosity, μ_l (kg m^{-1} s^{-1})	0.006
Stefan–Boltzmann constant, σ (W m^{-2} K^{-4})	5.67×10^{-8}
Electrical conductivity, σ_e (Ω^{-1} m^{-1})	7.14×10^{-5}
Density of liquid phase, ρ_l (kg m^{-3})	6900
Density of plasma, ρ_{pl} (kg m^{-3})	0.06
Density of solid phase, ρ_s (kg m^{-3})	7200

2.1.3.1. Top surface inside the keyhole (AE in Fig. 1). For cells containing free surface, that is, cells that contain fluid but have one or more empty neighbors, in the direction normal to the free surface, the following pressure condition must be satisfied [28]:

$$P = P_\sigma + P_r \tag{9}$$

where P is the pressure at the free surface in a direction normal to the local free surface. P_σ is the surface tension and P_r is the recoil pressure. P_σ is calculated by the following formula:

$$P_\sigma = \kappa\gamma \tag{10}$$

where κ is the free surface curvature, given by [26]:

$$\kappa = -\left[\nabla\cdot\left(\frac{\vec{n}}{|\vec{n}|}\right)\right] = \frac{1}{|\vec{n}|}\left[\left(\frac{\vec{n}}{|\vec{n}|}\cdot\nabla\right)|\vec{n}| - (\nabla\cdot\vec{n})\right] \tag{11}$$

where $\vec{n}$ is the unit vector normal to the local free surface. For a pseudo-binary *Fe-S* system, the surface tension coefficient γ can be calculated as a function of temperature T and sulfur concentration f^α [29]:

$$\gamma = 1.943 - 4.3\times10^{-4}(T-1723) - RT\times1.3\times10^{-8} \times \ln\left[1 + 0.00318 f^\alpha \exp\left(\frac{1.66\times10^8}{RT}\right)\right] \tag{12}$$

In this study, the sulfur concentration is assumed to be constant, and the temperature-dependent Marangoni shear stress on the free surface in the direction tangential to the local surface is given by [30]:

$$\tau_{\vec{s}} = \mu_1\frac{\partial(\boldsymbol{V}\cdot\vec{s})}{\partial\vec{n}} = \frac{\partial\gamma}{\partial T}\frac{\partial T}{\partial\vec{s}} \tag{13}$$

Calculation of the evaporation-induced recoil pressure P_r is complicated by the existence of a Knudsen layer over the vaporizing surface. Based on Knight's model [31], the recoil pressure can be calculated by [32]:

$$P_r = AB_0/\sqrt{T_\mathrm{w}}\exp(-U/T_\mathrm{w}) \tag{14}$$

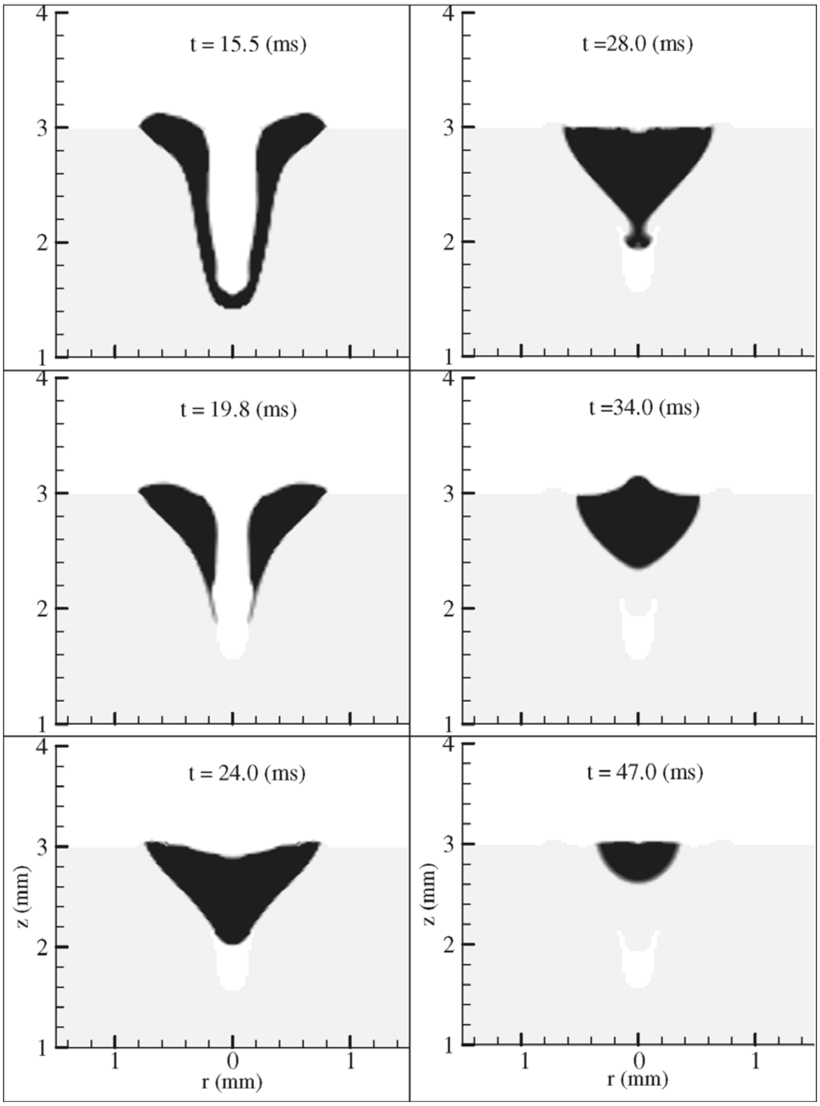

Fig. 2. A figure shows the porosity formation process in pulsed laser keyhole welding [12] (laser power is 1.7 kW and pulse duration is 15.0 ms).

where A is the numerical coefficient and B_0 is the vaporization constant. The coefficient A depends on the ambient pressure and its value varies from 0.55 for evaporation in the vacuum to 1 for the case of evaporation under a high ambient pressure. For atmospheric pressure, the coefficient A is close to its minimal value of 0.55. B_0 is at the value of 1.78×10^{10}. T_w is the surface temperature of the liquid metal on the keyhole wall. The parameter U is defined as follows [32]:

$$U = m_a H_v / (N_a k_b) \tag{15}$$

where m_a is the atomic mass, H_v is the latent heat of evaporation, N_a is the Avogadro's number and k_b is the Boltzmann constant.

The energy on the top free surface is balanced between the laser irradiation, plasma-keyhole wall radiation, the heat dissipation through convection, and metal vaporization. In general, since the velocity of the plume along the surface is assumed to be zero [24], the heat loss due to convection is omitted. The energy balance is given by the following formula:

$$k\frac{\partial T}{\partial \vec{n}} = q_{\text{laser}} + q_{\text{rad}} - q_{\text{evap}} \tag{16}$$

In this study, the liquid/vapor evaporation model is used due to the low intensity of laser irradiation. The heat loss due to surface evaporation can be written as [33]

$$q_{\text{evap}} = WH_v \tag{17}$$

$$\log(W) = A_v + \left(6.121 - \frac{18836}{T}\right) - 0.5\log T \tag{18}$$

The laser heat flux q_{laser} comes from the Fresnel absorption of the incident intensity directly from the laser beam plus the incident intensity from the multiple reflections:

$$q_{\text{laser}} = I_0(r,z)\alpha_{\text{Fr}}(\varphi_0) + \sum_{m=1}^{n} I_{r,m}(r,z)\alpha_{\text{Fr}}(\varphi_m) \tag{19}$$

$$\alpha_{\text{Fr}}(\varphi) = 1 - \frac{1}{2}\left(\frac{1+(1-\varepsilon_f\cos\varphi)^2}{1+(1+\varepsilon_f\cos\varphi)^2} + \frac{\varepsilon_f^2 - 2\varepsilon_f\cos\varphi + 2\cos^2\varphi}{\varepsilon_f^2 + 2\varepsilon_f\cos\varphi + 2\cos^2\varphi}\right) \tag{20}$$

where ϕ is the angle of the incident light with the normal of the keyhole surface, n is the total number of incident light from multiple reflections. ε_f is a material-dependent coefficient. In CO_2 laser welding of mild steel, $\varepsilon_f = 0.2$ is used. $I_0(r,z)$ and $I_{r,m}(r,z)$ are, respectively, the incident intensity from the laser beam and the mth multiple reflection at the keyhole wall which are given as

$$I_0(r,z) = I_c(r)\exp\left(-\int_0^{z_0} K_{\text{pl}}\,\mathrm{d}z\right) \tag{21}$$

$$I_{r,m}(r,z) = I_r(r,z)\exp\left(-\int_0^{z_m} K_{\text{pl}}\,\mathrm{d}z\right) \tag{22}$$

$$I_r(r,z) = I_0(r,z)(1-\alpha_{\text{Fr}}) \tag{23}$$

where $I_c(r)$ stands for the original collimated incident laser beam intensity, $I_{r,m}(r,z)$ is the reflected laser beam intensity at the m times reflections, $\int_0^{z_0} K_{\text{pl}}\,\mathrm{d}z$ and $\int_0^{z_m} K_{\text{pl}}\,\mathrm{d}z$ are the optical thickness of the laser transportation path, respectively, for the first incident and the multiple reflections, and K_{pl} is the plasma absorption coefficient due to the inverse Bremsstrahlung (IB) absorption [34]

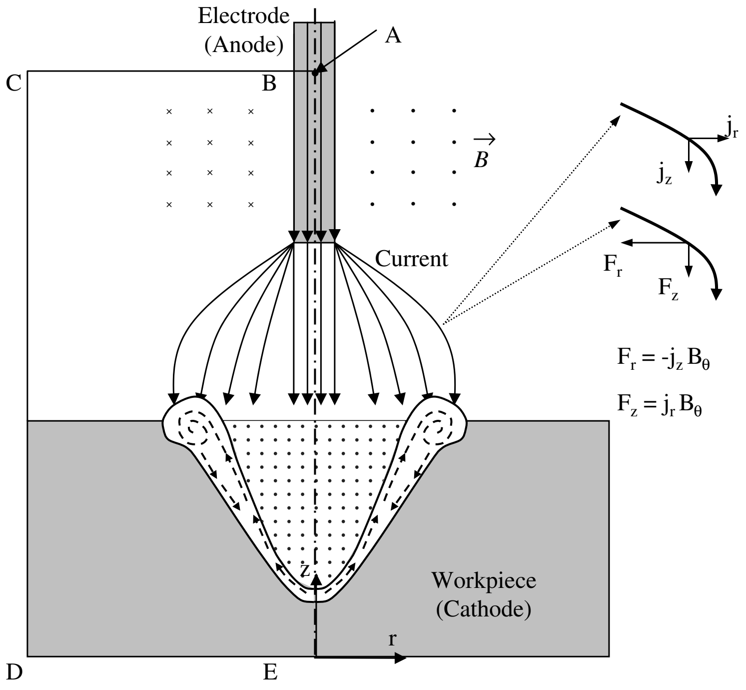

Fig. 3. A figure used to explain the direction and magnitude of electromagnetic force.

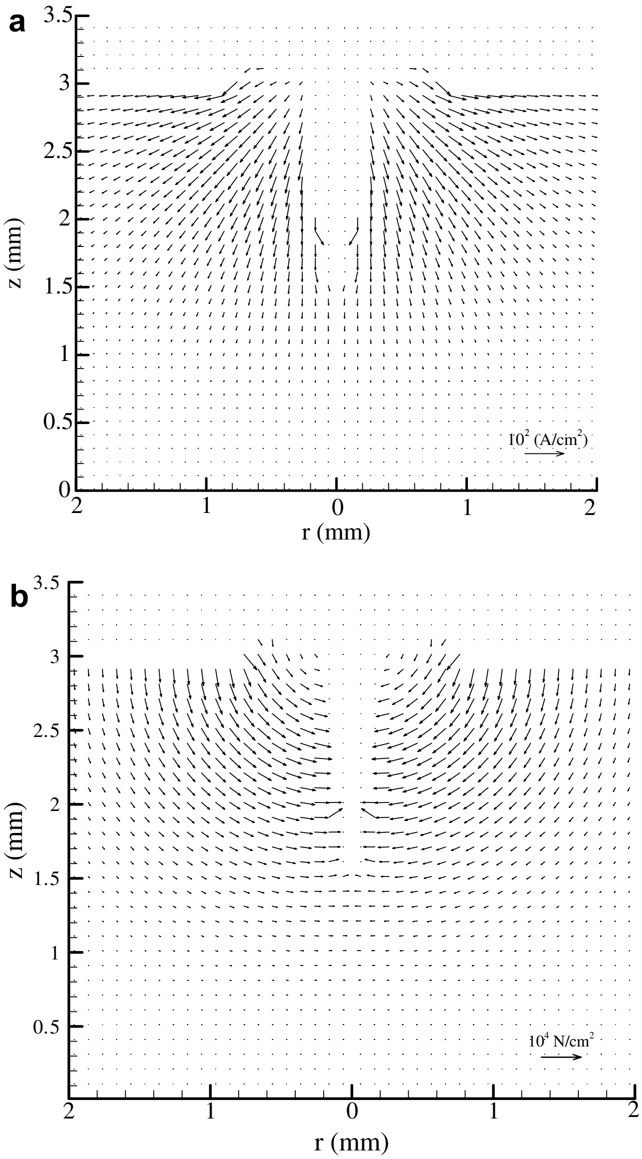

Fig. 4. The calculated (a) current density vector (b) electromagnetic force vector distributions at $t = 19.2$ ms ($I = 30$ A and $B_0 = 300$ mT).

$$K_{\mathrm{pl}} = \frac{n_{\mathrm{e}} n_{\mathrm{i}} Z^2 e^6 2\pi}{6\sqrt{3} m \varepsilon_0^3 c \bar{h} \omega^3 m_{\mathrm{e}}^2} \left(\frac{m_{\mathrm{e}}}{2\pi k_{\mathrm{b}} T_{\mathrm{pl}}}\right)^{0.5} \left[1 - \exp\left(-\frac{\omega}{k_{\mathrm{b}} T_{\mathrm{pl}}}\right)\right] \bar{g} \tag{24}$$

where Z is the charge of ion in the plasma, e is the charge of electron, ω is the angular frequency of the laser irradiation, ε_0 is the dielectric constant, n_{e} and n_{i} are the densities of electrons and ions, respectively, $\bar{h}$ is the Planck's constant, m is a constant that is related to the specific laser being used and is 1 for CO_2 laser, m_{e} is the electron mass, T_{pl} is the plasma temperature, c is the speed of light, and $\bar{g}$ is the quantum mechanical Gaunt factor. For weakly ionized plasma in the keyhole, Saha equation [35] can be used to calculate the densities of the plasma species:

$$\frac{n_{\mathrm{e}} n_{\mathrm{i}}}{n_0} = \frac{g_{\mathrm{e}} g_{\mathrm{i}}}{g_0} \frac{(2\pi m_{\mathrm{e}} k_{\mathrm{b}} T_{\mathrm{pl}})^{1.5}}{\bar{h}^3} \exp\left(-\frac{E_{\mathrm{i}}}{k_{\mathrm{b}} T_{\mathrm{pl}}}\right) \tag{25}$$

where n_0 is neutral particle density which is $10^{26}/\mathrm{cm}^3$ for iron [35], g_{e}, g_{i} and g_0 are, respectively, the degeneracy factors for electrons, ions and neutral atoms, E_{i} is the ionization potential for the neutral atoms in the gas. Assuming the laser intensity distribution, $I_{\mathrm{c}}(r)$, is ideal Gaussian-like and can be written as [36]

$$I_{\mathrm{c}}(r) = \frac{2P_{\mathrm{laser}}}{\pi r_{\mathrm{fo}}^2} \left(\frac{r_{\mathrm{f}}}{r_{\mathrm{fo}}}\right)^2 \exp\left(-\frac{2r^2}{r_{\mathrm{f}}^2}\right) \tag{26}$$

where r_{f} is the beam radius, r_{fo} is the beam radius at the focal position, and P_{laser} is the laser power. In laser welding, the keyhole surface temperature is much lower than that of the plasma, so the radiation and emission of the surface can be omitted. Then q_{rad} can be simplified as

$$q_{\mathrm{rad}} = \varepsilon\sigma(\overline{T_{\mathrm{pl}}}^4 - T^4) \tag{27}$$

where $\overline{T_{\mathrm{pl}}}$ is the average temperature of keyhole plasma.

2.1.3.2. *Top surface outside the keyhole (AB in Fig. 1).*

Boundary condition on the top surface outside the keyhole is similar to that inside the keyhole. The differences lie in the absence of plasma and multiple reflections. As shown in Fig. 1, there is a shielding gas flow above the base metal, which means that plasma outside the keyhole will be blown away. So Eq. (19) can be written as

$$q_{\mathrm{laser}} = I_0(r,z)\alpha_{\mathrm{Fr}} \cos\varphi \tag{28}$$

Since there is no plasma and the temperature of shielding gas is much lower than that of the metal surface, the radiation heat flux can be given as

$$q_{\mathrm{rad}} = -\varepsilon\sigma(T^4 - T_\infty^4) \tag{29}$$

Here, T_∞ is the ambient temperature. Since there is a shielding gas flow over the surface, the convection heat loss cannot be omitted which is given by

$$q_{\mathrm{conv}} = h_{\mathrm{conv}}(T - T_\infty) \tag{30}$$

2.1.3.3. *Side surface (BC in Fig. 1).*

$$-k\frac{\partial T}{\partial r} = q_{\mathrm{conv}} \tag{31}$$

$$u = 0, \quad v = 0 \tag{32}$$

2.1.3.4. *Bottom surface (CD in Fig. 1).*

$$-k\frac{\partial T}{\partial z} = q_{\mathrm{conv}} \tag{33}$$

$$u = 0, \quad v = 0 \tag{34}$$

2.1.3.5. *Symmetrical axis (DE in Fig. 1).*

$$\frac{\partial T}{\partial r} = 0 \tag{35}$$

$$u = 0, \quad \frac{\partial v}{\partial r} = 0 \tag{36}$$

The boundary conditions for the calculation of Eq. (6) are listed in Table 1.

2.2. Plasma zone simulation

2.2.1. Governing equations

In current study, metal vapor in the keyhole is assumed to be a compressible, inviscid ideal gas. Since the heat production by viscous dissipation is rather small in laser welding, the energy equation can be simplified as [37]:

$$\frac{\partial}{\partial t}(\rho_{\mathrm{pl}} h_{\mathrm{pl}}) = \nabla \cdot \left(\frac{k_{\mathrm{pl}}}{c_{\mathrm{pl}}} \nabla h_{\mathrm{pl}} - \boldsymbol{q}_r\right) + K_{\mathrm{pl}} I_{\mathrm{c}}(r) \exp\left(-\int_0^{z_0} K_{\mathrm{pl}}\,\mathrm{d}z\right) + \sum_{m=1}^{n} K_{\mathrm{pl}} I_{r,m}(r,z) \exp\left(-\int_0^{z_m} K_{\mathrm{pl}}\,\mathrm{d}z\right) \tag{37}$$

where h_{pl} and ρ_{pl} represent, respectively, the enthalpy and density of the plasma, k_{pl} and c_{pl} represent, respectively, the thermal conductivity and specific heat of the plasma. $\boldsymbol{q}_r$ stands for the radiation heat flux vector. Note $h_{\mathrm{pl}} = c_{\mathrm{pl}} T_{\mathrm{pl}}$.

The radiation source term $\nabla \cdot (\boldsymbol{q}_r)$ is defined as

$$\nabla \cdot \boldsymbol{q}_r = k_{\mathrm{a}}\left(4\pi I_{\mathrm{b}} - \int_{4\pi} I\,\mathrm{d}\Omega\right) \tag{38}$$

where k_{a}, I_{b} and Ω denote the Planck mean absorption coefficient, blackbody emission intensity ($I_{\mathrm{b}} = \sigma T_{\mathrm{pl}}^4$) and solid angle, respectively. When an intense laser pulse interacts with the vapor in the keyhole, a significant amount of laser irradiation is absorbed by the ionized particles through the IB absorption. For simplicity, the plasma is assumed to be an absorbing-emitting medium and the scattering effect is neglected. The radiation transport equation (RTE) has to be solved for the total directional radiative intensity $\boldsymbol{I}(\boldsymbol{r},\boldsymbol{s})$ [38]

$$(\boldsymbol{s} \cdot \nabla) I(\boldsymbol{r},\boldsymbol{s}) = k_{\mathrm{a}}(I_{\mathrm{b}} - I(\boldsymbol{r},\boldsymbol{s})) \tag{39}$$

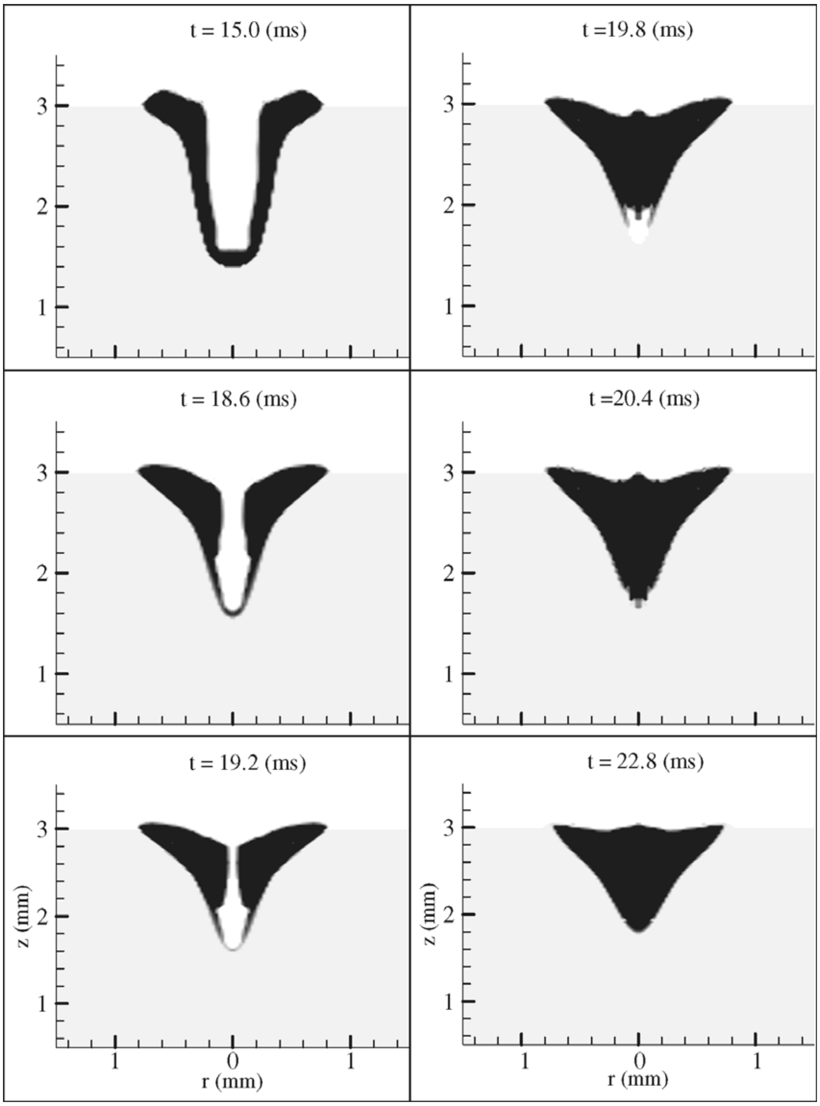

Fig. 5. The liquid metal evolution for a medium depth-to-width ratio keyhole.

where ***s*** and ***r*** denote a unit vector along the direction of the radiation intensity and the local position vector. When the plume within the keyhole is weakly ionized, the absorption mechanism mainly depends on electron-neutral interaction and the plume behaves as an optically thin medium. For the evaluation of the intensity and heat flux divergence, the Planck mean absorption coefficient is given as [38]

$$k_{\mathrm{a}} = \left(\frac{128}{27}k_{\mathrm{b}}\right)^{0.5}\left(\frac{\pi}{m_{\mathrm{e}}}\right)^{1.5}\frac{Z^2e^6\bar{g}}{h\sigma c^3}\,\frac{n_{\mathrm{e}}n_{\mathrm{i}}}{T_{\mathrm{pl}}^{3.5}} \tag{40}$$

2.2.2. Boundary conditions

2.2.2.1. Bottom surface inside the keyhole (EA in Fig. 1). Close to the liquid wall inside the keyhole, there is a so-called Knudsen layer where vaporization of material takes place. The vapor temperature across the Knudsen layer is discontinuous, which can be calculated by the following formula [31]:

$$\frac{T_{\mathrm{K}}}{T_{\mathrm{l}}} = \left[\sqrt{1+\pi\left(\frac{\gamma_r-1}{\gamma_r+1}\frac{m_{\mathrm{v}}}{2}\right)^2} - \sqrt{\pi}\frac{\gamma_r-1}{\gamma_r+1}\frac{m_{\mathrm{v}}}{2}\right]^2 \tag{41}$$

$$m_{\mathrm{v}} = M_k\sqrt{\frac{2}{\gamma_r}} \tag{42}$$

where T_{K} is the vapor temperature outside of the Knudsen layer, T_{l} is the liquid surface temperature adjacent to the Knudsen layer, M_k is Mach number at the outer of the Knudsen layer and γ_r is the specific heat ratio. The value of m_{v} depends on the gas dynamics of the vapor flow away from the surface. $M_k = 1.2$ is used in the present study [31]. The vapor is assumed to be iron in the form of monatomic gas with molecular weight of 56 and $\gamma_r = 1.67$. The gas tem-

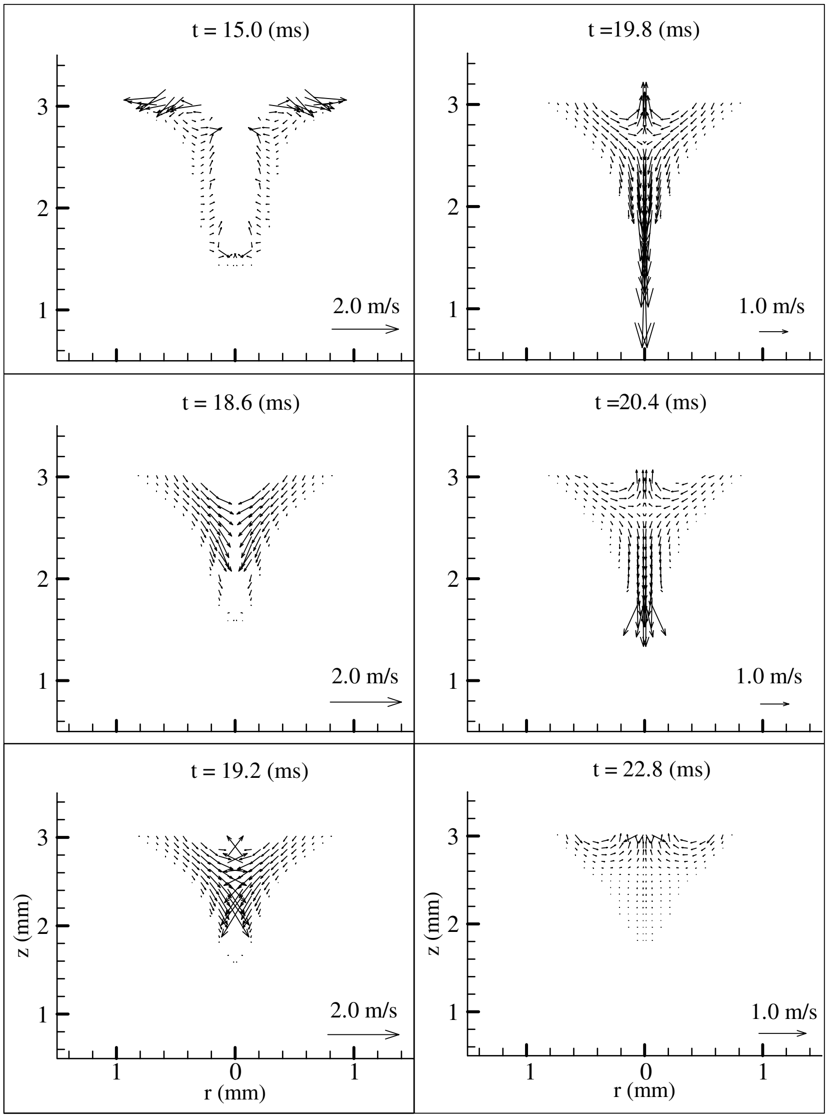

Fig. 6. The corresponding velocity distributions as shown in Fig. 5.

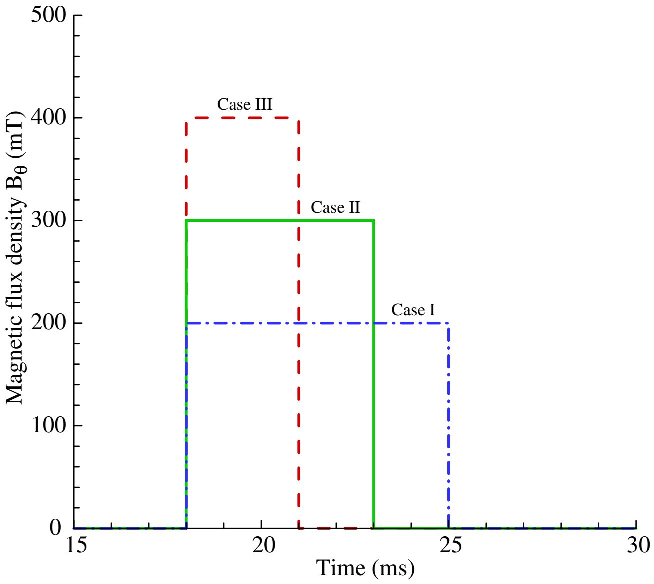

Fig. 7. Magnetic flux used in porosity prevention for a large depth-to-width ratio keyhole.

perature outside the Knudsen layer is used as the boundary temperature. So the boundary condition is given by [38]:

$$T_{\mathrm{pl}} = T_{\mathrm{K}} \tag{43}$$

$$I = \varepsilon I_{\mathrm{b}} + \frac{1-\varepsilon}{\pi}\int_{\vec{n}\cdot\Omega'<0} I|\vec{n}\cdot\Omega|\,\mathrm{d}\Omega' \tag{44}$$

2.2.2.2. Top surface outside the keyhole (FA in Fig. 1).

$$T_{\mathrm{pl}} = T_{\infty} \tag{45}$$

$$I = I_{\mathrm{c}}(r) \tag{46}$$

2.2.2.3. Symmetrical axis (EF in Fig. 1).

$$\frac{\partial T_{\mathrm{pl}}}{\partial r} = 0 \tag{47}$$

$$\frac{\partial I}{\partial r} = 0 \tag{48}$$

3. Numerical method

The solutions of transport equations in the metal zone and in the plasma zone are coupled; that is, the simulations of the metal and the plasma zone provide boundary conditions for each other. However, there are large spatial and physical differences between the metal and the plasma zone. To enhance convergence rate and save calculation time, different time and space resolutions are used for the metal and the plasma zone. The governing equations (Eqs. (1)–(4), (6) and (37)) and all related supplemental equations and boundary conditions are solved through the following iterative scheme:

1. Eqs. (1)–(4) are solved iteratively for the metal zone to obtain velocity, pressure and temperature distributions using the associated boundary conditions.
2. Eq. (37) is solved iteratively to obtain the plasma temperature distributions in the keyhole under the associated boundary conditions. The steps for solving Eq. (37) are listed below:
   (a) Solve Eq. (39) using the associated boundary conditions to get the total directional radiative intensity distributions.
   (b) Solve Eq. (38) to get radiation source term $\nabla\cdot(\boldsymbol{q}_r)$.
   (c) Solve Eqs. (25) and (24) in the order using the most recent plasma temperature from the previous time step to get the updated plasma absorption coefficient K_{pl}.
   (d) Solve Eq. (37) to get the updated plasma temperature.
3. Solve VOF algorithm equation (8) to obtain the new domain for the metal and plasma zones.
4. Update boundary conditions for the metal and the plasma zones.
5. Eq. (6) and the associated boundary conditions are solved to obtain current density in the *r*- and *z*-directions. Then, Eq. (7) and Eq. (5) were solved for electromagnetic force.
6. Advance to the next time step and back to Step 1 until the desired time is reached.

In the calculation, before electromagnetic force is applied, there is no electromagnetic force term in Eqs. (2) and (3) and, hence, the calculation of electromagnetic force, Step 5, is skipped.

The techniques for solving Eqs. (1)–(4) and (37) are given by Wang and Tsai [26]. Following the MAC scheme, the *r*- and *z*-velocity components are located at cell face centers on lines of constants *r* and *z*, respectively; while the pressure, VOF function, temperature and absorbed laser flux are located at cell centers. Since the temperature and pressure field change more dramatically near the keyhole, a non-uniform grid system with 202 × 252 points is used for the total computational domain of 5.0 mm × 20.0 mm, in which smaller grids are concentrated near the keyhole and larger grids for other parts. Due to the axis-symmetry of the domain, only half of the grid points were used in the calculation. Calculations were executed on the DELL OPTIPLEX GX270 workstations with LINUX-REDHAT 9.0 OS and it took about 6 h of CPU time to simulate about 100 ms of real-time welding. The average time step is 10^{-4} s and the smallest time step is about 10^{-6} s.

4. Results and discussion

The base metal is assumed to be 304 stainless steel. The process parameters and thermophysical properties used in the present study are summarized in Table 2. The laser

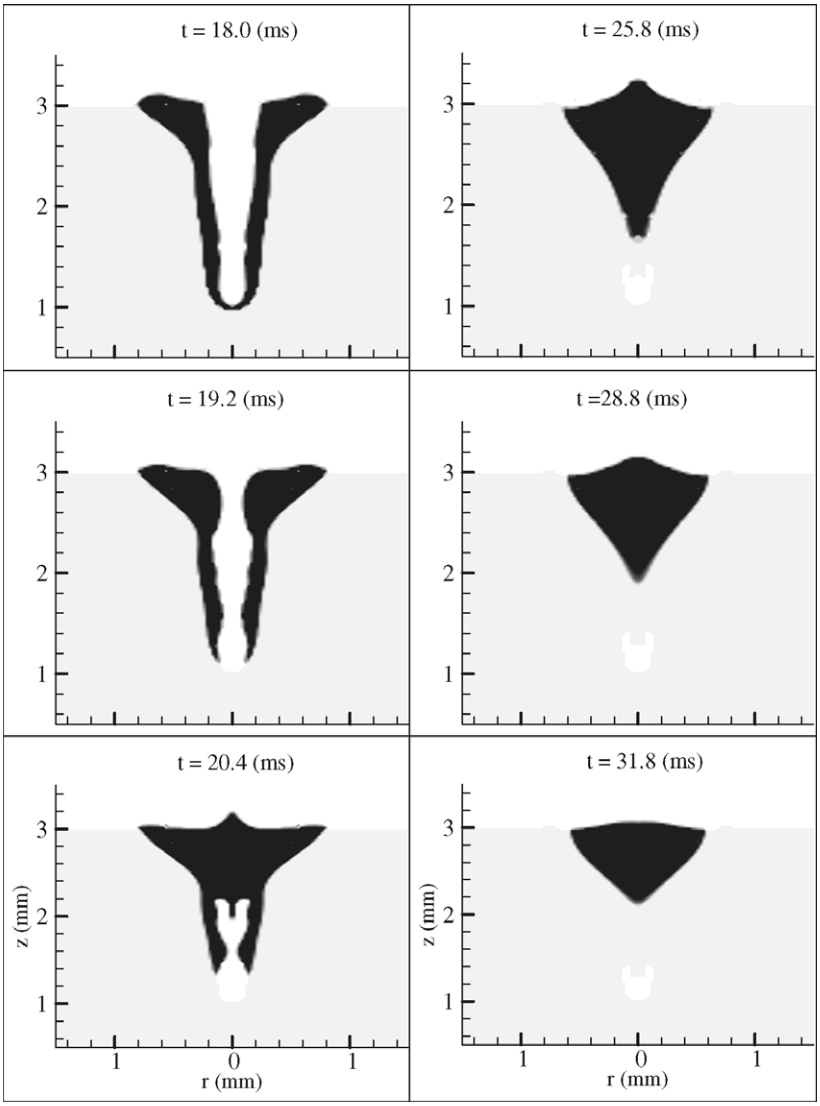

Fig. 8. The liquid metal evolution for a large depth-to-width ratio keyhole; Case I: small electromagnetic force.

energy is assumed to be in Gaussian distribution and the focus plane is on the top surface of the base metal. The laser irradiation duration varies in different study cases. As the present study focuses on how the keyhole is back filled during the keyhole collapse process, the keyhole formation process is omitted and the temperature distributions of the liquid metal and the plasma in the keyhole are also omitted and they can be found in Ref. [11].

4.1. Application of electromagnetic force in laser keyhole welding

Porosity formation mechanism and its prevention by pulse control have been discussed before [8,9,12]; hence, the following discussion will be focused on the studies of increasing the back filling speed of melt flow to prevent porosity formation in pulsed laser welding. Fig. 2 shows a typical porosity formation process in pulsed laser welding which is reproduced from Ref. [12] to facilitate the following discussion. As shown in the figure at $t = 28.0$ ms, the back filling liquid metal from the top is blocked by the solidification near the bottom of the keyhole. Hence, in order to eliminate porosity, the back filling speed of the liquid metal must be high enough to reach the bottom of the keyhole before complete solidification. This can be achieved by exerting an external force to accelerate the back filling speed of the liquid metal. It is well known that when an electric field interacts with a magnetic field, an electromagnetic body force (Lorentz force) will be generated. Since steel is an electrically conductive material, electromagnetic body force $\boldsymbol{J} \times \boldsymbol{B}$ can be introduced in laser welding to “stir” the weld pool to increase the back filling speed of the liquid metal during the keyhole collapse process.

This idea is briefly shown in Fig. 3. In the figure, j_r and j_z are, respectively, the electric current field distribution in the r- and z-direction; B_0 is the applied external magnetic flux; and F_r and F_z are, respectively, the electromagnetic forces in the r- and z-direction. In the model, an external electric current $\boldsymbol{J}$ is applied via an electrode above the workpiece when the laser irradiation is shut off. The two components of current, j_r and j_z are, calculated via Eq. (7). Since the self-induced magnetic field generated by this electric current is relatively small (as compared to the externally applied magnetic field), in order to intensify the electromagnetic body force in the weld pool, a DC electromagnet is employed to generate a homogeneous magnetic field B_θ in the direction as shown in Fig. 3. The magnitudes and durations of the electric current and magnetic field vary in different study cases. Fig. 4 shows typical calculated electric current density distribution and electromagnetic force distribution in a pulsed laser keyhole welding process at $t = 19.2$ ms and $I = 30$ A and $B_\theta = 300$ mT. As shown in Fig. 4(a), the electric current is flowing downward and outward in the base metal which will result in an inward and downward electromagnetic force as shown in Fig. 3. This is verified by the electromagnetic force distribution shown in Fig. 4(b). This downward and inward electromagnetic force can increase the downward and inward momentum of the liquid metal and is helpful in eliminating porosity discussed in the following.

4.2. Porosity prevention by electromagnetic force

4.2.1. Medium depth-to-width aspect ratio keyhole

For the same welding conditions used to produce the results shown in Fig. 2, an external current 30 A and a constant magnetic flux $B_\theta = 300$ mT are applied as soon as the laser irradiation is shut off (at 15 ms) and they last for 5 ms. Fig. 5 shows the liquid metal evolution during the keyhole collapse process, and the corresponding velocity distribution is shown in Fig. 6. Note in order to increase readability, only one-half of the grid nodes are used for plotting the velocity distribution. At $t = 15.0$ ms, after the laser power is shut off, the recoil pressure is gone and the liquid metal near the top of the keyhole has a tendency to flow

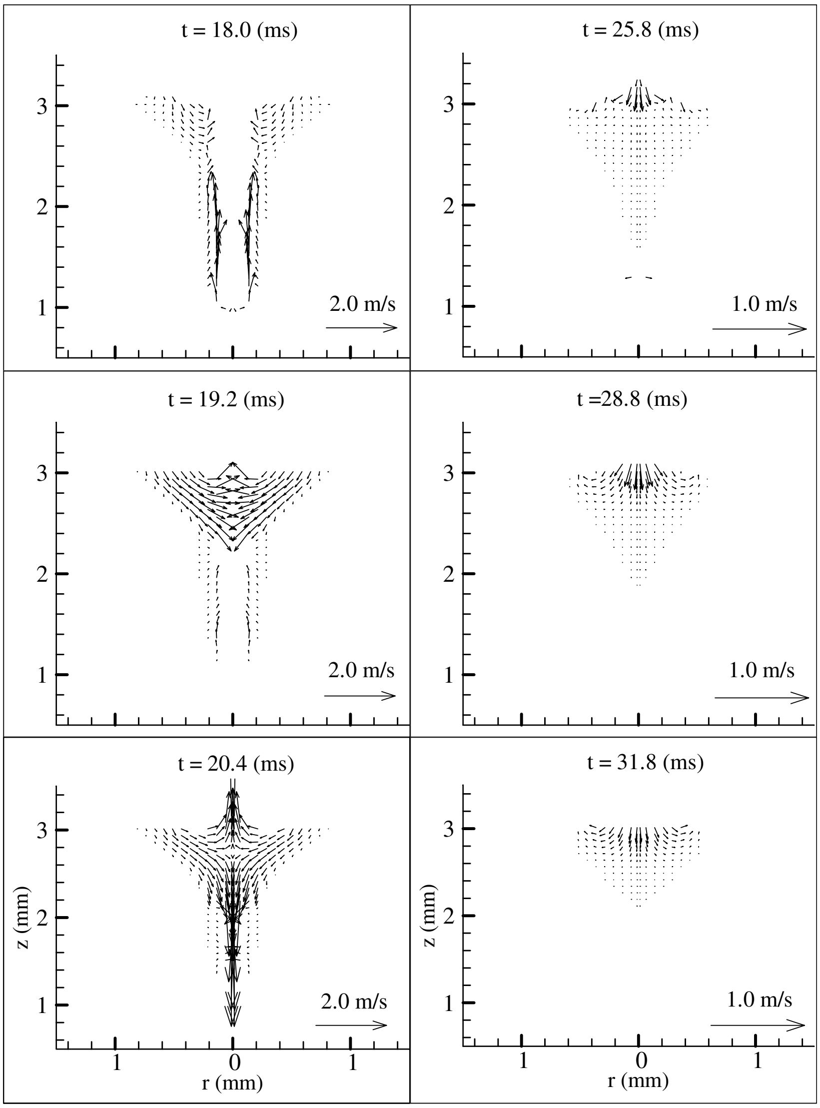

Fig. 9. The corresponding velocity distributions as shown in Fig. 8.

downward to fill the keyhole under the action of gravity and surface tension. As the electromagnetic force is downward and inward, it will enhance the gravity and surface tension and shorten the time for the liquid metal to backfill the keyhole. As shown in Figs. 5 and 6 from $t = 15.0$ ms to $t = 18.6$ ms, the downward and inward velocities of the melt flow in the keyhole change more quickly than those without electromagnetic force, shown in Fig. 2. This is especially true for the liquid metal near the shoulder of the keyhole; the inward electromagnetic force "sweeps" the molten metal surrounding the top of the keyhole into the keyhole. Comparing Figs. 5 and 2, it is seen that the keyhole is filled earlier for the case with the applied electromagnetic force.

As shown in Fig. 5, the liquid–solid interface (i.e., solidification front) moves inward and upward from the keyhole in the metal after the laser irradiation is terminated. As the electromagnetic force is greater near the top of the keyhole (see Fig. 4(b)) and much less liquid metal exists near the bottom of the keyhole than that on the shoulder, the effect of electromagnetic force on the liquid metal near the bottom is not as remarkable as on that near the top of the keyhole. Hence, the application of electromagnetic force has little influence on the solidification rate of the liquid metal near the bottom of the keyhole. By comparing Figs. 5 and 2, at $t = 19.8$ ms, it is seen the liquid metal still quickly solidifies near the bottom of the keyhole even when electromagnetic force is being applied. However, the downward velocity of liquid metal continues to be accelerated by electromagnetic force and the bottom of the keyhole at $t = 20.4$ ms is filled before complete solidification. Hence, at $t = 22.8$ ms, there is no pore/void formed in the final weld.

4.2.2. Large depth-to-width aspect ratio keyhole

As discussed before, the formation of porosity in laser welding is strongly related to the depth-to-width aspect ratio of the keyhole [12]. The larger the ratio, the easier

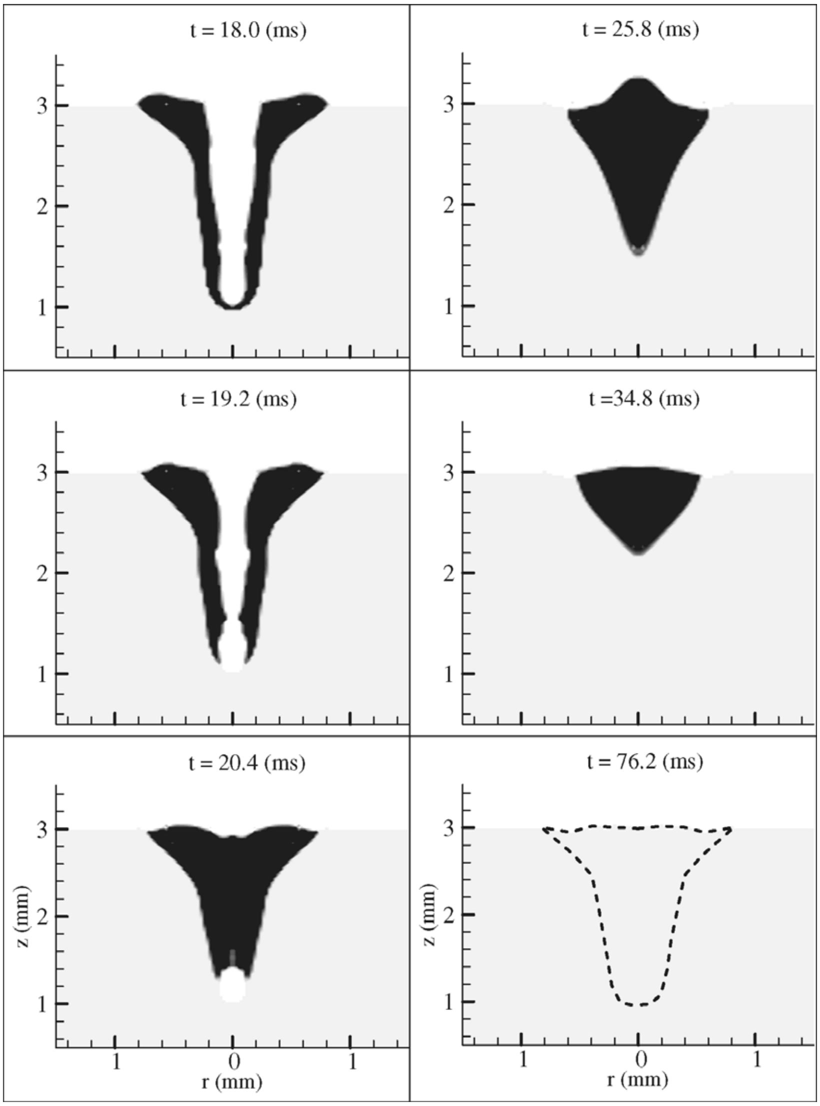

Fig. 10. The liquid metal evolution for a large depth-to-width ratio keyhole; Case II: medium electromagnetic force.

the porosity can be formed. In order to prevent the porosity at the root of the keyhole in the large depth-to-width aspect ratio laser keyhole welding process, the back filling speed of the liquid metal must be accelerated faster than that in the medium ratio pulsed laser keyhole welding process. In the following, the effects of the strength of electromagnetic force and its duration on melt flow and porosity formation will be discussed. The electric current used in these study cases are all at 30 A, while the magnitude and duration of the external magnetic flux vary as shown in Fig. 7. Based on the relative magnitude of the magnetic flux, in the following discussion we designate small, medium, and large electromagnetic force, respectively, for Case I, Case II, and Case III.

Case I: Small electromagnetic force. The liquid metal evolution and corresponding velocity distribution are shown in Figs. 8 and 9. In this case, the electromagnetic force is applied at 18.0 ms right after the turn-off of the laser power and is held for 7.0 ms. Similar to that shown in Fig. 4(b), the direction of the electromagnetic force is inward and downward.

Under the action of electromagnetic force, the liquid metal on the top flows inward and downward to quickly refill the keyhole after the shut-off of the laser beam, as shown in Fig. 9. In this case, the keyhole is deeper, which means it requires a longer time for the liquid metal from the top to reach the bottom of the keyhole. Since the magnitude of electromagnetic force is relatively small in this case, the back filling speed of the liquid metal could not be accelerated high enough to reach the bottom of the keyhole before complete solidification. This process is shown in Fig. 8. As shown, the bottom of the back filling liquid metal solidifies at the depth of about 1.6 mm. After that,

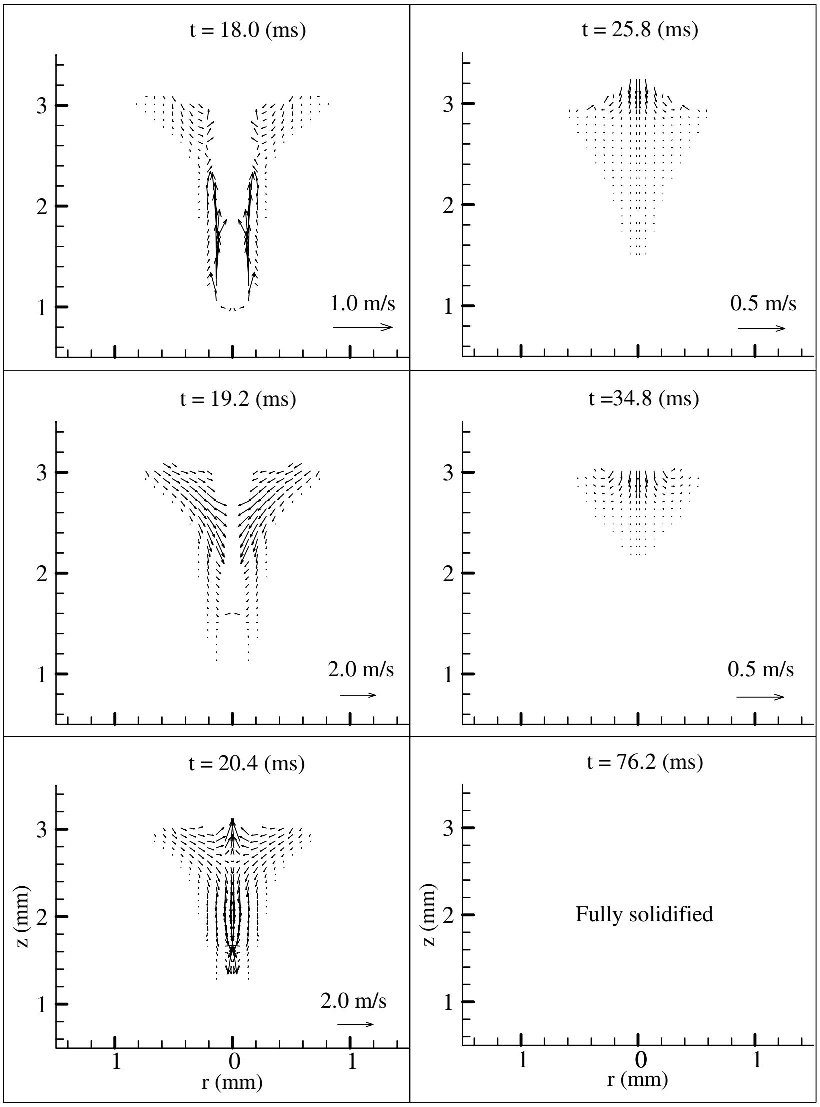

Fig. 11. The corresponding velocity distributions as shown in Fig. 10.

although there is still some liquid metal on the top, it was blocked by the solidified metal and could not flow farther to reach the bottom of the keyhole. Hence, a pore/void was found at the root of the keyhole, though the size of the pore/void is smaller than that shown in the case without the use of an electromagnetic force.

Case II: Medium electromagnetic force. In this case, the magnetic flux B_0 is increased to 300 mT and the duration of the magnetic field is 5.0 ms, as shown in Fig. 7. The liquid metal evolution and the corresponding velocity distribution are shown in Figs. 10 and 11, respectively.

As shown in Fig. 11, since the magnitude of the applied electromagnetic force is increased, the back filling speed of the liquid metal from the top is faster than that shown in Fig. 9. Due to the strong downward momentum induced by the downward electromagnetic force, the liquid metal on the top quickly flows downward and reaches the bottom of the keyhole before complete solidification. As shown in Fig. 10 at $t = 25.8$ ms, the keyhole was completely filled up by the liquid metal and the pore/void at the root of the keyhole was eliminated. Also, as shown in Fig. 10 at $t = 25.8$ ms, an extrusion was found in the center of the weld pool. This is due to the strong inward push of the liquid metal by the electromagnetic force. However, under the action of the hydrostatic force and surface tension, this squeezed liquid metal is able to flow back to the edge of the keyhole before complete solidification. The completely solidified weld pool is shown by a dashed curve at $t = 76.2$ ms.

Case III: Large electromagnetic force. In this case, the magnetic flux B_0 is increased to 400 mT and its duration is decreased to 3.0 ms, as shown in Fig. 7. The liquid metal evolution and the corresponding velocity distribution are illustrated in Figs. 12 and 13, respectively. Since the magni-

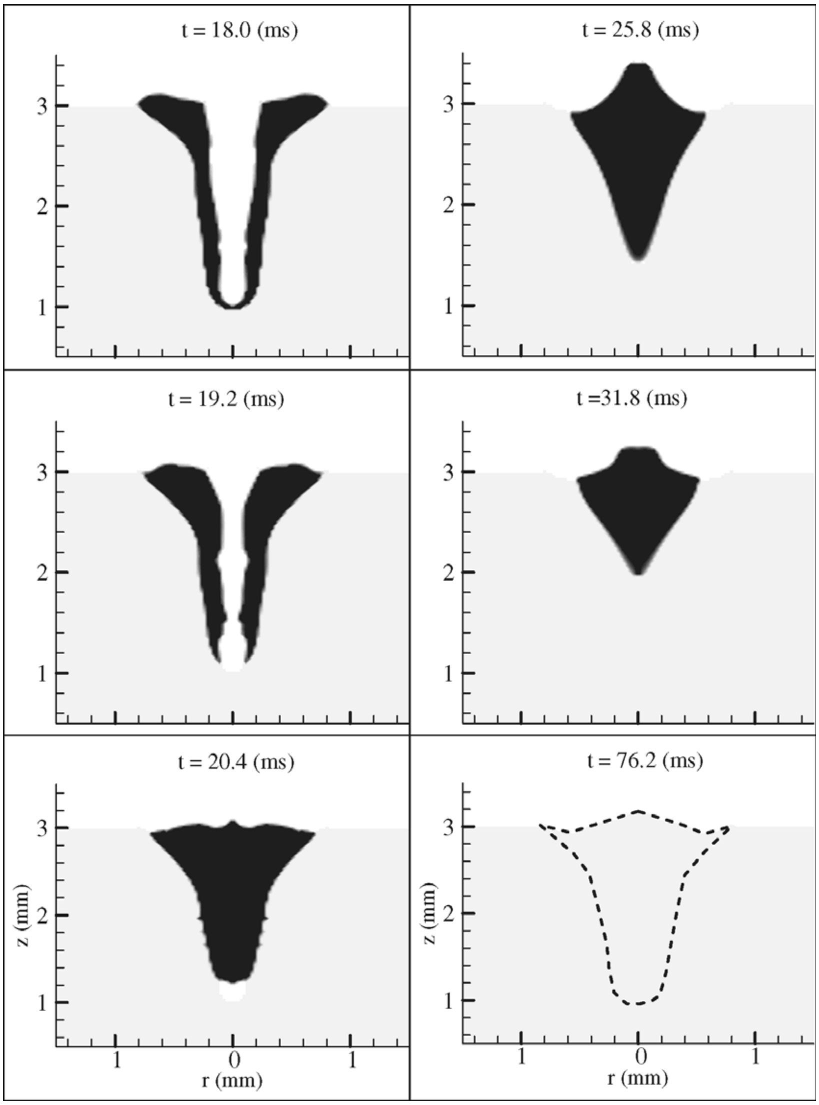

Fig. 12. The liquid metal evolution for a large depth-to-width ratio keyhole; Case III: large electromagnetic force.

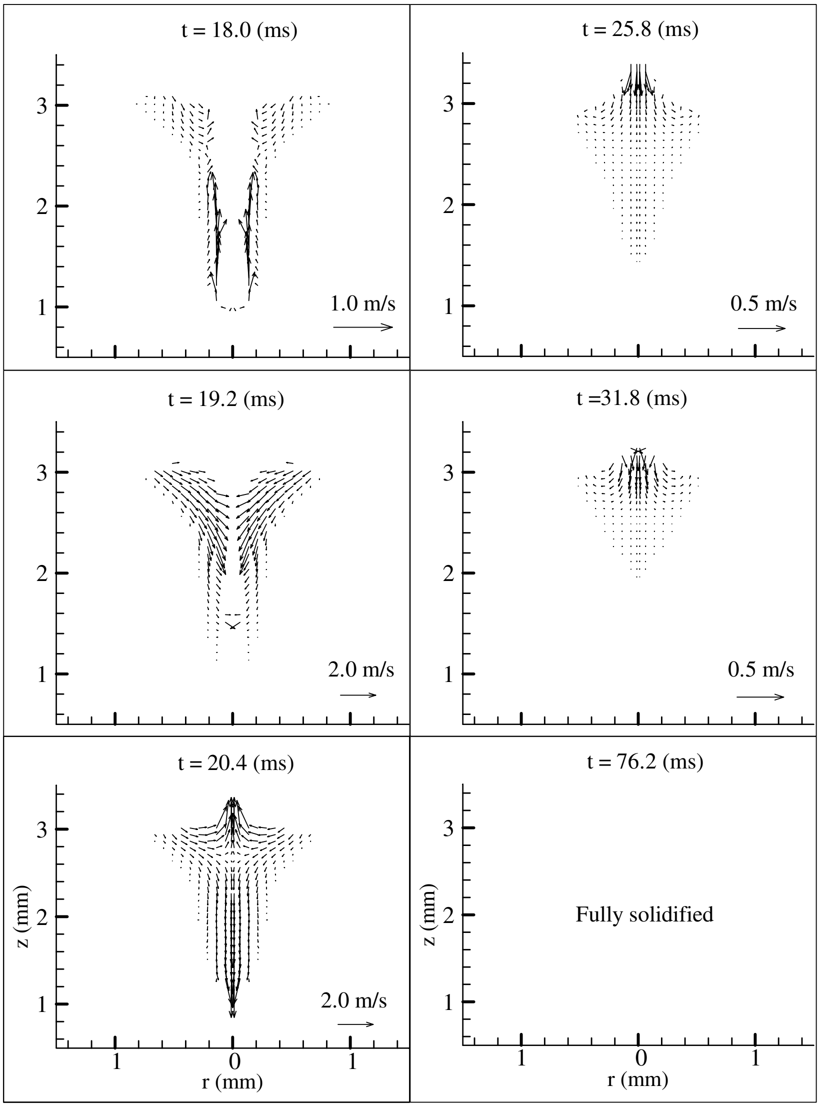

Fig. 13. The corresponding velocity distributions as shown in Fig. 12.

tude of electromagnetic force is greater, as shown in Fig. 13 at $t = 19.2$ ms, the downward velocity of the liquid metal is greater than that in Fig. 11. This strong electromagnetic force pushes the liquid metal from the top to flow downward to fill up the keyhole much faster than those in the previous two cases. As shown in Fig. 12 at $t = 20.4$ ms, the liquid metal from the top almost completely fills up the keyhole. Hence, the pore/void at the bottom of the keyhole caused by rapid solidification after the shut-off of the laser power [12] is eliminated.

Although this greater electromagnetic force can help prevent porosity formation at the root of the keyhole more easily, it can cause some other welding defects. As shown in Fig. 13, at $t = 20.4$ ms, the inward velocity of the liquid metal becomes very strong due to the strong inward push from this large electromagnetic force that squeezes the liquid metal upward, as shown in Fig. 13 at $t = 25.8$ ms. Even though electromagnetic force is turned off at $t = 21.0$ ms, since the upward momentum of the liquid metal is so strong, it takes a relatively longer time for the hydrostatic force and surface tension to even the liquid metal. At this time, since the solidification proceeds quite fast, the liquid metal flowing from the center to the edge quickly solidifies. The final weld shape is indicated by a dashed-curve at $t = 76.2$ ms. It is clearly seen the undercuts at the edge and an extrusion in the center of the final weld. Hence, for the given welding conditions and the resulting keyhole as discussed above, the Case II medium electromagnetic force can be considered to be the optimum to achieve quality welds.

5. Conclusions

Mathematical models have been developed to investigate the effects of electromagnetic force on porosity prevention in pulsed laser keyhole welding. The formation of porosity is strongly related to two competing factors: one is the liquid metal solidification rate and the other is the back filling speed of the liquid metal. If the back filling speed of the liquid metal on the upper part of the keyhole is not large enough to be able to reach the bottom of the keyhole, porosity will be found in the final weld.

The use of an external electromagnetic force can increase the back filling speed of the liquid metal during the keyhole collapse process. It allows the liquid metal from the upper part of the keyhole to reach the bottom of the keyhole in a short period of time. As shown in the present study, for a medium depth-to-width aspect ratio laser keyhole welding process, applying an electromagnetic force is a very effective way to prevent porosity formation. While for a large depth-to-width aspect ratio laser keyhole, the strength of the applied electromagnetic force and its duration are critical to prevent/eliminate porosity formation and to prevent the formation of undercuts. When the applied electromagnetic force is too big, although porosity at the root of the keyhole can be eliminated, other welding defects, such as extrusion in the center and undercuts at the edge of the final weld, can be formed in final welds. If an optimal electromagnetic force is applied, porosity can be eliminated and good quality welds can be achieved for a high depth-to-width aspect ratio laser keyhole welding process.

Acknowledgement

It is gratefully acknowledged that this work is partially supported by the General Motors Corporation.

References

[1] S. Katayama, N. Seto, J. Kim, A. Matsunawa, Formation mechanism and reduction method of porosity in laser welding of stainless steel, in: Proc. of ICALEO Sec. G, 1997, pp. 83–92.

[2] S. Katayama, N. Seto, J. Kim, A. Matsunawa, Formation mechanism and suppression procedure of porosity in high power laser welding of aluminum alloys, in: Proc. of ICALEO Sec. C, 1998, pp. 24–33.

[3] S. Katayama, A. Matsunawa, Formation mechanism and prevention of defects in laser welding of aluminum alloys, in: Proc. of CISFFEL 6, vol. 1, 1998, pp. 215–222.

[4] T. Ishide, S. Tsubota, M. Nayama, Y. Shimokusu, T. Nagashima, K. Okimura, 10 kW class YAG laser application for heavy components, in: SPIE High-power Lasers in Manufacturing, vol. 3888, Osaka, 1999, pp. 543–550.

[5] S. Katayama, N. Seto, M. Mizutani, A. Matsunawa, Formation mechanism of porosity in high power YAG laser welding, in: Proc. of ICALEO Sec. C, 2000, pp. 16–25.

[6] N. Seto, S. Katayama, A. Matsunawa, A high-speed simultaneous observation of plasma and keyhole behavior during high power CO_2 laser welding, in: Proc. of ICALEO Sec. E, 1999, pp. 17–19.

[7] S. Katayama, S. Kohsaka, M. Mizutani, K. Nishizawa, A. Matsunawa, Pulse shape optimization for defect prevention in pulsed laser welding of stainless steels, in: Proc. of ICALEO, 1993, pp. 487–497.

[8] S. Katayama, Y. Kobayashi, N. Seto, M. Mizutani, A. Matsunawa, Effect of vacuum on penetration and defects in laser welding, in: Proc. of ICALEO Sec. C, 2000, pp. 182–191.

[9] S. Tsukamoto, I. Kawaguchi, G. Arakane, Suppression of welding defects in deep penetration CO_2 laser welding, in: Proc. of ICALEO Sec. C, 2000, pp. 7–15.

[10] A. Todate, Y. Ueno, M. Katsuki, S. Katayama, A. Matsunawa, YAG laser weldability of carbon steel in CO_2 shielding gas, in: Proc. of the National Meeting of JWS 66, 2000, pp. 144–145.

[11] J. Zhou, H.L. Tsai, P.C. Wang, Transport phenomena and keyhole dynamics during pulsed laser welding, ASME J. Heat Transfer 128 (7) (2006) 680–690.

[12] J. Zhou, H.L. Tsai, Porosity formation and prevention in pulsed laser welding, ASME J. Heat Transfer, in press.

[13] R. Sampath, N. Zabaras, Adjoint variable method for the thermal design of eutectic directional solidification processes in an open-boat configuration, Numer. Heat Transfer Part A: Appl. 32 (6) (2001) 655–683.

[14] E. Goncalves, M. Faghri, Y. Asako, M. Charmchi, Numerical solution of melting processes for unfixed phase-change material in the presence of electromagnetically simulated low gravity, Numer. Heat Transfer Part A: Appl. 46 (4) (2004) 343–365.

[15] E. Goncalves, M. Faghri, Y. Asako, M. Charmchi, Numerical solution of melting in side-heated rectangular enclosure under electromagnetically simulated low gravity, Numer. Heat Transfer Part A: Appl. 47 (4) (2005) 315–332.

[16] Y. Manabe, H. Wada, H. Kondou, Y. Hiromoto, Y. Kobayashi, International Institute of Welding, IIW–XII, 1997, pp. 1484–1497.

[17] G.M. Shelenkov, Weld. Production 3 (1997) 24–25.

[18] S. Kou, Y.H. Wang, Computer simulation of convection in moving arc weld pools, Metall. Trans. 17A (1986) 2271–2277.

[19] W.-H. Kim, H.G. Fang, S.-J. Na, Effect of various driving forces on heat and mass transfer in arc welding, Numer. Heat Transfer Part A: Appl. 32 (6) (1997) 633–652.

[20] M. Kern, P. Berger, H. Hugel, Magneto-fluid dynamic control of seam quality in CO_2 laser beam welding, Weld. J. 79 (3) (2000) 72s–78s.

[21] D. Lindenau, G. Ambrosy, P. Berger, H. Hugel, Effects of magnetically supported laser beam welding of aluminum alloys, in: ICALEO Sec. A, 2001, pp. 308–318.

[22] D.B. Kothe, R.C. Mjolsness, M.D. Torrey, Ripple: A Computer Program for Incompressible Flows with Free Surfaces, LA-12007-MS, Los Alamos National Laboratory, 1991.

[23] K.C. Chiang, H.L. Tsai, Shrinkage-induced fluid flow and domain change in two-dimensional alloy solidification, Int. J. Heat Mass Transfer 35 (1992) 1763–1769.

[24] I. Miyamoto, E. Ohmura, T. Maede, Dynamic behavior of plume and keyhole in CO_2 laser welding, in: Proc. ICALEO Sec. G, 1997, pp. 210–218.

[25] J. Dowden, N. Postacioglu, M. Davis, P. Kapadia, A keyhole model in penetration welding with a laser, J. Phys. D: Appl. Phys. 20 (1987) 36–44.

[26] Y. Wang, H.L. Tsai, Impingement of filler droplets and weld pool dynamics during gas metal arc welding process, Int. J. Heat Mass Transfer 44 (2001) 2067–2080.

[27] J. Hu, H.L. Tsai, Heat and mass transfer in gas metal arc welding. Part I: the arc, Int. J. Heat Mass Transfer, in press, doi:10.1016/j.ijheatmasstransfer.2006.08.025.

[28] W. Duley, Laser Welding, John Wiley & Sons Inc, 1999.

[29] P. Sahoo, T. DeBroy, M.J. Mcnallan, Surface tension of binary metal-surface active solute systems under conditions relevant to welding metallurgy, Metall. Trans. 19B (1988) 483–491.

[30] R.T.C. Choo, J. Szekely, S.A. David, On the calculation of the free surface temperature of gas-tungsten-arc weld pools from first principles: part II. Modeling the weld pool and comparison with experiments, Metall. Trans. 23B (1992) 371–384.

[31] C.J. Knight, Theoretical modeling of rapid surface vaporization with back pressure, AIAA J. 17 (1979) 519–523.

[32] V. Semak, A. Matsunawa, The role of recoil pressure in energy balance during laser materials processing, J. Phys. D: Appl. Phys. 30 (1997) 2541–2552.

[33] T. Zacharia, S.A. David, J.M. Vitek, Effects of evaporation and temperature-dependent material properties on weld pool development, Metall. Trans. 22B (1991) 233–241.

[34] Yu.P. Raizer, Laser-induced Discharge Phenomena, Consultants Bureau, New York, 1977.

[35] L. Spitzer, Physics of Fully Ionized Gases, Interscience Publishers, New York, 1967.

[36] H. Kogelnik, T. Li, Laser beams and resonators, Appl. Opt. 5 (10) (1966) 1550–1554.

[37] R. Siegel, J.R. Howell, Thermal Radiation Heat Transfer, third ed., Hemisphere Publishing Corp, 1992 (Chapter 13).

[38] R. Ho, C.P. Grigoropoulos, J.A.C. Humphrey, Gas dynamics and radiation heat transfer in the vapor plume produced by pulsed laser irradiation of aluminum, J. Appl. Phys. 79 (1996) 7205–7215.